

Decay of the ^{112}Sn compound nucleus: Excitation functions of evaporation residues, energy spectra, and angular distributions of evaporated protons and alphas

Bency John and S. K. Kataria

Nuclear Physics Division, Bhabha Atomic Research Centre, Mumbai, India 400085

B. S. Tomar, A. Goswami, G. K. Gubbi, and S. B. Manohar

Radiochemistry Division, Bhabha Atomic Research Centre, Mumbai, India 400085

(Received 9 April 1997)

Evaporation residue excitation functions of the reaction $^{19}\text{F} + ^{93}\text{Nb} \rightarrow ^{112}\text{Sn}^*$, in the bombarding energy range between 54 and 95 MeV, have been measured using the recoil catcher technique. Energy spectra, angular distributions, and correlations between angular anisotropy and ejectile energy of evaporated protons and alpha particles have been measured for the above system at 73 and 95 MeV bombarding energies. The experimental data are compared with the predictions of the statistical model code PACE2 making use of two different level density formalisms. The level density parameters derived from the proton and alpha spectra are presented. The angular-anisotropy ejectile-energy correlations of the alpha particles show a peak in the variation of the anisotropy with the ejectile energy in the subevaporation barrier range. The sensitivity of the angular-anisotropy ejectile-energy correlations to the statistical model parameters is discussed. [S0556-2813(97)03811-9]

PACS number(s): 25.70.Gh, 25.70.Jj, 21.10.Ma, 27.60.+j

I. INTRODUCTION

Heavy ion fusion reactions are characterized by the deposition of a large amount of energy and angular momentum into the compound nucleus. Understanding the relaxation of such an excited nucleus is a subject of wide interest. An excited compound nucleus will decay predominantly by the emission of neutrons, protons, alpha particles, and gamma rays or by the nuclear fission, and all these decay channels compete with each other. The deexcitation of the compound nucleus thus encounters a range of excitation energy, spins, and intermediate nuclei. According to the statistical model of nuclear reactions, the actual course of deexcitation is determined by the statistical decay probabilities of the various decay modes at various stages of the decay. The basic ingredients used, for modeling the deexcitation on the basis of the statistical decay probabilities, include the density of levels of the final states, and the barrier penetration factors. Although a large volume of experimental data exists which ascertain the statistical nature of the compound nucleus decay [1], questions related to the choice of the basic parameters in the statistical model calculations are often asked.

The identification and cross section measurement of the final products of the deexcitation, namely, the evaporation residues (ER's), provides a quantitative survey of all the particle decay modes of the compound nucleus. Since the mass numbers of the ER's are decided at a later stage of the evaporation cascade where the shell effects are significant, their measurements are particularly important to study the shell structure effects on the level density. Therefore, the comparison of ER cross sections over a wide range of initial excitation energies with that predicted from a statistical model calculation, is expected to provide a testing ground for the excitation energy dependence of the shell effects incorporated in the calculation. Furthermore, the energy spectra and the angular distributions of the light charged particles evapo-

rated from the excited nuclei, provide details about the statistical model parameters. The near and below effective-barrier part of the spectra is strongly influenced by the barrier transmission coefficients (T_l) [2,3]. This part is also sensitive to the yrast region of the (E^*, J) plane [2]. The part of the spectra well above the effective-barrier energies is less sensitive to the T_l 's but is very sensitive to the spin dependent level density of the emitting nucleus [3]. The angular distributions of the evaporated particles are related to the rotational energy and the temperature of the emitting nucleus [4]. By demanding a consistent reproduction of the experimental ER excitation functions and the evaporated particle spectra and/or averaged properties by the statistical model calculations, one can hope to answer some of the questions regarding the choice of the basic parameters. This possibility has received much attention recently in the study of ER survival probabilities to determine the dynamical properties of fissionable compound nuclei [5].

Although the ER excitation functions and the charged particle energy spectra under a variety of conditions were studied extensively in the past, a complete understanding has not yet emerged. This is particularly true for the case of heavy ion reactions where high excitation energies and high spin states are populated. The complexity of the underlying physical processes increases if large deformations are present in the emitting nuclei and/or large number of particles are evaporated [2,3,5]. By limiting to spherical systems, one can hope to investigate the evaporation process avoiding some complexity. Even for such systems, the choice of the parameters are uncertain. For instance, take the case of level density parameter a_{LDM} experimentally derived from the spectra of light charged particles. Chbihi *et al.* [6] reported different values of a_{LDM} for different particles emitted from highly excited nuclei in the mass region $A \sim 110$. In a recent work, in the same mass and excitation energy region, Gomez *et al.*

[7] observed that different values of the temperature T , or a_{LDM} , are required to characterize the evaporated light charged particle spectra. The angular distribution studies are also not free of controversies. Nicolis *et al.* [2], reported widely different angular distributions for the alpha particles from heavy ion reactions leading to $^{110}\text{Sn}^*$ and $^{114}\text{Sn}^*$ compound nuclei, which obscured a clear understanding about the role of the statistical model parameters in deciding them.

More precise measurements of the ER excitation functions, particle energy spectra, and angular distributions together with a comparison with improved statistical model calculations thus assume significance. Therefore, we have measured the excitation functions for ER's, and the energy and angular distributions of protons and alpha particles in the reaction $^{19}\text{F} + ^{93}\text{Nb} \rightarrow ^{112}\text{Sn}^*$. Experimental correlations between the angular anisotropy and the ejectile energy of protons and the alpha particles have been obtained. The data were analyzed using the statistical model code PACE2 [9] using a consistent set of parameters.

For the present system, in the chosen energy range, the compound nuclear reaction leading to $^{112}\text{Sn}^*$, accounts for the major part of the reaction cross section. This compound nucleus is expected to be spherical in shape due to the proton shell closure. Several experimental studies on the shape effects of excited $^{110}\text{Sn}^*$ [2,8], and $^{114}\text{Sn}^*$ [2] nuclei support this expectation. The PACE2 code is equipped to calculate the emission properties of spherical systems. In the present excitation energy region, the proton and alpha multiplicities are less than unity and as a result, long decay chains involving these particles in the later stages, are not expected to occur. Therefore, the extrapolation procedure adopted in the PACE2 code, for calculating the transmission coefficients for the exit channels, will not introduce much uncertainty. In the present version of PACE2, there are two options for the level density formula: The modified Gilbert-Cameron (GC) formula [9,10] and the Kataria-Ramamurthy-Kapoor (KRK) formula [11]. The relative advantages of the two formulas in treating the shell effects can thus be studied.

In the PACE2 code, the initial angular momentum distribution for the compound nucleus is calculated from the values of L_{max} and ΔL (diffuseness) parameters [9]. Elastic scattering data and its optical model analysis can provide approximate value of the ΔL . By using the ΔL and the systematics of fusion cross sections compiled by Bass *et al.* [12], one can fix the compound nucleus angular momentum distribution reasonably well. With this aim, we have measured the elastic scattering angular distributions of $^{19}\text{F} + ^{93}\text{Nb}$ system at 73 MeV and 95 MeV bombarding energies. The data were analyzed using the optical model, and the values of ΔL for the two bombarding energies were extracted.

The present article is organized in the following way. The experimental procedures for elastic scattering, ER excitation function, and proton and alpha energy and angular distribution measurements are presented in Sec. II. The results are presented in Sec. III. A discussion on the results is given in Sec. IV. Finally, the summary and conclusions are presented in Sec. V.

II. EXPERIMENTAL PROCEDURES

The experiments were performed using the BARC-TIFR pelletron accelerator facility at Mumbai. The elastic scatter-

ing and the proton/alpha particle spectra were measured in separate experiments. A set of calibrated surface barrier detector telescopes and the general purpose scattering chamber were used for these measurements. For the ER excitation function measurement, off line recoil-catcher technique was employed. The details of the experimental procedures are described in the following subsections.

A. Elastic scattering

The elastic scattering measurements were carried out using ^{19}F beam at 73 and 95 MeV bombarding energies. The beam current ranged from 5 to 15 nA. The target was a self-supporting foil of niobium metal prepared by rolling. The thickness of the target was determined by energy loss measurement using an Am-Pu-Cm composite alpha source. Using the stopping power tables of Northcliffe and Schilling [13], the thickness of the target was estimated to be $700 \mu\text{g m/cm}^2$. The elastically scattered ^{19}F ions were detected using two well-collimated surface barrier detectors, having thicknesses around $250 \mu\text{m}$ and subtending equal solid angles of 0.24 msr. The angular distributions were measured in the θ_{lab} range from 20° to 105° . A monitor detector subtending a solid angle of 0.04 msr was mounted at $\theta_{\text{lab}} = 15^\circ$ for the Rutherford normalization. The elastic scattering data normalized to the Rutherford cross sections are shown in Fig. 1(a) as closed circles, for both the bombarding energies. The statistical error in the measured cross section values are around $\pm 3\%$ for the forward angles, and it progressively increases to $\pm 10\%$ for the backward angles.

B. Evaporation residue excitation function

The ER excitation function measurements were carried out using the foil stack irradiation facility. In each irradiation, one foil stack, comprising of a pair of metallic niobium target foils backed by recoil catcher foils, was bombarded with ^{19}F beam. The niobium targets were prepared by rolling and were having thicknesses $\sim 1.0 \text{ mg/cm}^2$. The recoil catchers were either 2 mg/cm^2 thick aluminum foils or 4 mg/cm^2 thick gold foils. Their thicknesses were sufficient to stop all recoiling evaporation residues emerging from the targets placed immediately in front. This arrangement of foils enabled to cover two bombarding energies in one irradiation. The bombarding energy on the first target was calculated by subtracting the energy loss suffered in the half thickness of the target, from the initial beam energy. The bombarding energy on the second target was calculated by subtracting the sum of the energy loss suffered by the beam in the first target and its catcher, and in the half thickness of the second target. The energy losses were calculated using the stopping power tables of Northcliffe and Schilling [13]. The energy straggling in the foils will cause some dispersions in the bombarding energies. The maximum width of the dispersions are expected to be around 1.5 MeV [31]. The corrections to the measured excitation functions due to the beam energy dispersions, therefore, are insignificant. The beam current was measured using an electron suppressed Faraday cup placed behind the foil stack. The bombarding energy range covered in all irradiations was from 54 MeV to 95 MeV. The irradiation times (t_0) were 10 min and 2 h for short-lived and long-lived products, respectively. After the

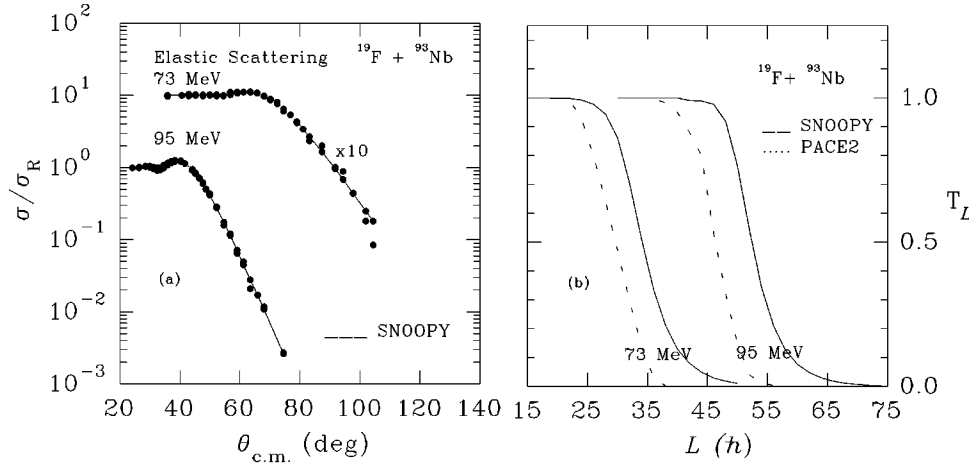


FIG. 1. (a) Elastic scattering angular distributions for 73 MeV, 95 MeV $^{19}\text{F} + ^{93}\text{Nb}$ system. The closed circles indicate the data. The continuous lines are optical model fits to the data obtained using the SNOOPY code [16]. (b) Transmission coefficients for the entrance channel (reaction T_L 's) vs L calculated using the parameters of above optical model fits (continuous lines). The fusion T_L values calculated using the Bass systematics for the fusion cross sections and $\Delta L = 1\hbar$ as a function of L , are shown as dashed lines.

irradiation, the target and the following catcher foil were together assayed for the gamma activities of the evaporation residues in two standard high purity germanium detectors. The detector active volumes were 80 cm^3 and 60 cm^3 . The detectors were calibrated for their efficiency and energy scale using a standard ^{152}Eu source. Their absolute detection efficiencies varied from about 10 to 0.9% for the gamma ray energy range from 121 keV to 1408 keV. The energy resolution of the detectors were around 2.0 keV at 1332 keV gamma ray energy. During the assay, the maximum count rate in the detectors was less than 10 000 cps. Hence, the pulse pileup effect which distorts the spectra was not significant for the present setup. The gamma spectra accumulated over a period of 10 days were analyzed using the code SAMPO [32] for extracting the photo peak areas. The peak areas thus obtained for the characteristic gamma ray of the specific ER were used to calculate the activity of the ER at the end of irradiation A_0 . The ER cross section (σ) was deduced from A_0 using the known values of target thickness (N), integrated beam current (ϕ), detector efficiency (ϵ_γ) and gamma ray abundance (I_γ) and the well-known relation

$$A_0 = N\sigma\phi[1 - \exp(-0.693t_0/T_{1/2})]I_\gamma\epsilon_\gamma, \quad (1)$$

where $T_{1/2}$ is the half-life of the ER. Table I lists the ER's for which the cross sections were measured in the present work. The gamma ray abundances and the half-lives are also given in Table I and were taken from the compilation of Reus and Westmeier [14]. The chosen gamma lines were ascertained to be free from the interference from any other γ - or x-ray lines by checking the half-life of each radionuclide. In case of $p\alpha n$ and $\alpha p\alpha n$ products, the gamma activities of the residues contain the contributions from β^+/EC decay of $(x+1)n$ and $\alpha(x+1)n$ products. These precursor contributions were taken into account and the cross sections reported are the independent formation cross sections for the specific channels.

C. Light charged particles

The measurements were carried out using ^{19}F beam at 73 MeV and 95 MeV bombarding energies. The target used was

a niobium metal foil (rolled) of thickness $450\ \mu\text{gm}/\text{cm}^2$. The detector system consisted of three well collimated silicon surface barrier $\Delta E - E$ telescopes mounted in the reaction plane. Telescope No. 1 (T1) comprised of a $22.8\ \mu\text{m}$ ΔE detector and a 1 mm E detector. Telescope No. 2 (T2) comprised of a $17\ \mu\text{m}$ ΔE detector and a 1 mm E detector. T1 and T2 were used for detecting particles with $Z \geq 2$ and had equal solid angles of 1.62 mSr. For detecting protons, Telescope No. 3 (T3) comprising of a $40\ \mu\text{m}$ ΔE detector and a 2 mm E detector and a having solid angle of 0.1 mSr, was used. T1 and T2 were calibrated using the alpha particles from an Am-Pu composite source and the elastically scattered ^{19}F ions detected at forward angles. T3 was calibrated using the recoiling protons from a thin mylar target on bombarding ^{19}F beam of energy 95 MeV. During the calibration, T3 was placed at various angles between 30° and 70° to detect proton peaks having well defined energy ranging from 2 to 13 MeV. Reference energies for the calibration of the telescopes thus cover the energy range of interest. During the data collection, the lower cutoffs for T1 and T2 were set electronically at ~ 4.7 MeV while for T3, the lower cutoff

TABLE I. Nuclear spectroscopic data used in this work.

Nuclide	Channel	Half-life	Energy (KeV)	Abundance I_γ (%)
^{109}Sn	$3n$	18.0 min	1321.3	12.3
^{108}Sn	$4n$	10.3 min	272.4	41.1
$^{109}\text{In}_g$	$p2n$	4.2 h	203.5	73.5
$^{108}\text{Sn}_m$	$p3n$	58.0 min	875.6	93.0
$^{107}\text{In}_g$	$p4n$	32.4 min	205.0	47.7
$^{106}\text{Ag}_m$	αpn	8.46 days	997.8	48.0
$^{105}\text{Ag}_g$	$\alpha p2n$	41.3 days	280.4	31.0
^{105}Cd	$\alpha 3n$	55.5 min	433.2	2.81
^{104}Cd	$\alpha 4n$	57.7 min	709.5	20.0

was set at ~ 1.5 MeV. During the data analysis, the lower cutoffs were set at slightly higher values, around 5 MeV for T1 and T2 and around 1.8 MeV for T3. The energy spectra measurements were carried out with T1 and T2 covering the θ_{lab} range from 20° to 160° and T3 covering the θ_{lab} range from 25° to 160° . Measurements at some of the angles were repeated with more than one telescope and the consistency of the data was confirmed. A monitor detector of surface barrier type (thickness $250 \mu\text{m}$) was mounted at $\theta_{\text{lab}}=20^\circ$ for the Rutherford normalization.

The impurities in the target are a matter of concern especially in the energy spectra measurements of light particles. The most important impurities responsible for the background protons and alphas were assessed to be carbon and oxygen. Since the oxide formation in niobium is much less owing to its low oxidation potential, the oxygen content in the target is expected to be much less than 1% by weight. Sufficient care was taken to use good vacuum conditions to minimize carbon deposition during the beam bombardment. As shown in [15], such efforts can limit the carbon impurity content to less than 1% by weight. For the present measurement, the presence of impurities was assessed to be less than or equal to 1% by weight. The extent of distortion to the energy spectra due to the background protons and alphas from such an amount of carbon impurity was estimated in the following way. The energy spectra of protons and alpha particles at various laboratory angles from $^{19}\text{F} + ^{93}\text{Nb}$ and $^{19}\text{F} + ^{12}\text{C}$ reactions were simulated using the PACE2 code. For a fixed bombarding energy of the ^{19}F ion, the proton and alpha spectra at various laboratory angles from the two reactions, were compared after scaling in the given proportion of the target amount. It was observed that the alpha background is negligibly small particularly for the backward angles. The proton background can slightly distort the spectra at some angles, however at the most backward angles, the background is negligible.

III. RESULTS

A. Elastic scattering

The measured elastic scattering cross sections for 73 MeV and 95 MeV bombarding energies [Fig. 1(a)] were analyzed using the phenomenological optical model code SNOOPY [16] in the parameter search mode. This code uses Woods-Saxon form for the real and imaginary potentials with the depth, radius, and diffuseness parameters of the potentials as the fitting parameters. The fits obtained are shown in Fig. 1(a) as continuous lines. The potential parameters and the reaction cross sections obtained for both the bombarding energies are listed in Table II. The transmission coefficients for the incident channels (T_L) as a function of the incident angular momentum L , calculated using SNOOPY, are shown in Fig. 1(b) as continuous lines for both the bombarding energies. The reaction cross sections derived from the above optical model analysis are listed in Table III.

The reaction cross sections include the incomplete fusion reactions (ICF's), in addition to the complete fusion reactions (CF's). In a separate work [17], we have measured the ICF reaction cross sections for the present system and the values obtained are listed in Table III. The complete fusion cross sections obtained by subtracting the ICF cross sections

TABLE II. Optical-model parameters for the $^{19}\text{F} + ^{93}\text{Nb}$ system.

Bombarding energy (MeV)	73	95
Real potential depth V (MeV)	46.5	54.6
Radius parameter (real) r_0 (fm)	1.25	1.25
Diffuseness (real) a_0 (fm)	0.501	0.508
Imaginary potential depth W (MeV)	36.0	42.2
Radius parameter (imaginary) r_i (fm)	1.25	1.25
Diffuseness (imaginary) a_i (fm)	0.498	0.478

from the reaction cross sections are also given in Table III. These cross sections are in reasonable agreement with the Bass systematics [12] of the fusion cross sections. The transmission coefficients for the fusion reactions, T_L 's, as a function of L , as calculated in the PACE2 code using the Bass systematics and $\Delta L = 1\hbar$, are shown in Fig. 1(b) as dashed lines. The diffuseness parameters, ΔL 's, in the reaction and fusion cases, are in mutual agreement for both the bombarding energies.

B. Evaporation residue excitation function

Figures 2(a)–2(i) show the measured excitation functions of the ER's. The ER symbols and the probable decay channels are indicated in each panel. The closed circles indicate the experimentally obtained values of the residue cross sections. The standard deviations on these values, on the average, are about 5%. The dashed lines indicate the theoretical estimates of cross sections obtained using the PACE2 code with the GC formula for the level densities. The continuous lines indicate the PACE2 estimates with the KRK formula. Apart from the differences in the level density formulas, all other parameters used in the two calculations were identical. The optical model parameters for the emitted light particle were taken from Huizenga and Igo [18], Perey [19], and Willmore and Hodgson [20] for alphas, protons, and neutrons, respectively. The average gamma transition strengths determined by Endt [21] for this mass region (0.000 02, 0.023, and 51.0 W.u for $E1$, $M1$, and $E2$, respectively) were used for the present calculations. The diffused surface nucleus moment of inertia was used for calculating the yrast lines. Experimentally known low lying levels of the six most probable residual nuclei were also used as input.

The main difference between GC and KRK formulas is in the method of incorporating the shell corrections to the energy dependent part of the level density. The GC formula

TABLE III. Some relevant cross sections of the $^{19}\text{F} + ^{93}\text{Nb}$ system.

Bombarding energy (MeV)	73	95
Reaction cross section (mb)	860 ± 60	1510 ± 90
ICF cross section (mb)	130 ± 10	290 ± 25
Fusion cross section (mb)	730 ± 62	1220 ± 93
Bass cross section (mb)	650	1150

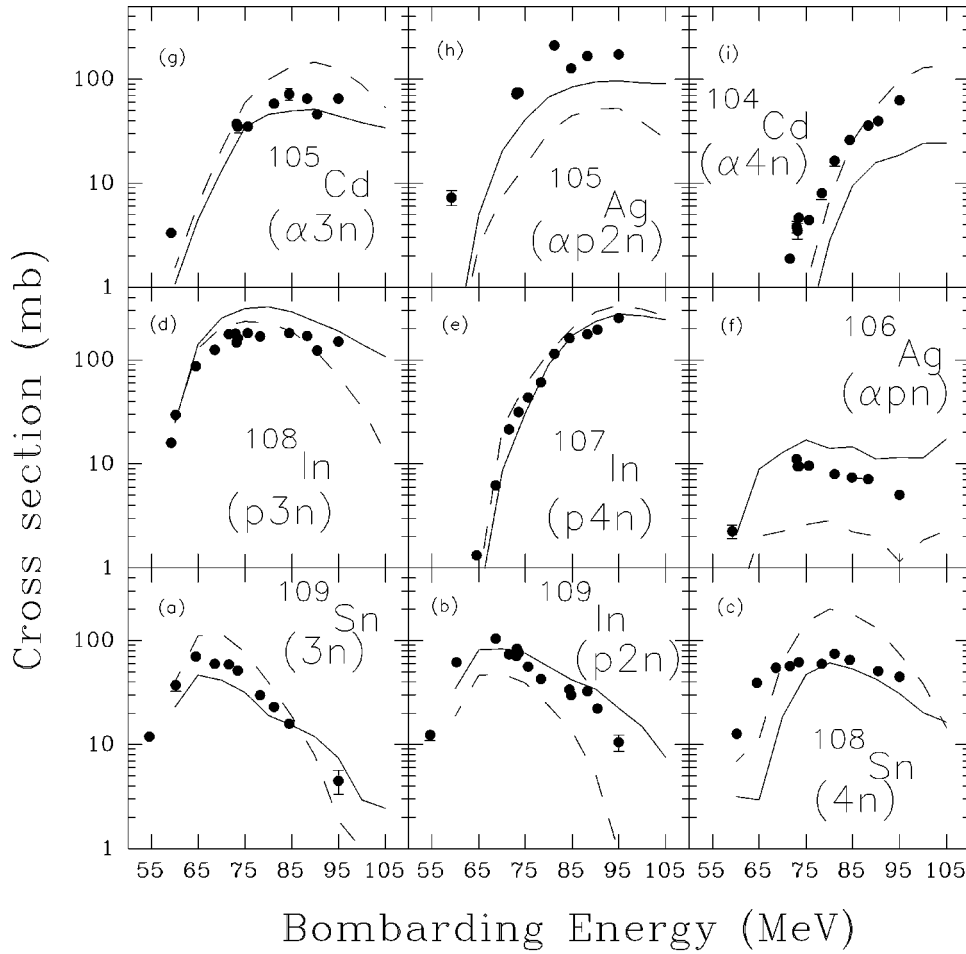


FIG. 2. (a)–(i) Experimental and calculated excitation functions of the evaporation residues (ER's) from the reaction $^{19}\text{F} + ^{93}\text{Nb}$. The closed circles indicate the experimental data. The ER symbols and the probable decay channels are indicated in each panel. The continuous and dashed lines are the PACE2 predictions with KRK level density formula, and GC level density formula, respectively.

achieves shell correction in two steps. For excitation energies below ~ 5 MeV, the constant temperature part of the formula accounts for the shell structure effects. For the entire range of excitation energies above ~ 5 MeV, the shell structure effects are accounted by the use of shell dependent value of a_{LDM} . However, the shell dependence used is applicable only at neutron resonance energies. Since the shell dependence of the thermodynamic behavior of the nucleus is excitation energy dependent, the GC approach is not entirely correct. This deficiency is corrected in the KRK formula by incorporating a built-in excitation energy dependence of the shell effects on the level densities. The KRK formula not only provides a good fit to the experimental data on neutron resonance spacings of spherical nuclei but also provides a reliable extrapolation to the higher excitation energies. In the asymptotic limit of high excitation energies, where the shell structure effects are washed out, the KRK formula provides an estimate of the level density which is consistent with the LDM estimate. For a detailed comparison of the GC and the KRK formulas, see [10,11,22]. In the present calculations for the ER excitation functions, the value of a_{LDM} used was $A/8$. As will be shown later, this value describes the above effective-barrier part of the experimental proton spectra, which is sensitive to a_{LDM} , quite well.

Visual inspection of Figs. 2(a)–2(i) and calculated squared deviations between the predictions and the data show that for all the residues barring ^{108}In and ^{104}Cd , the KRK predictions are in better agreement with the data com-

pared to the GC predictions. For ^{108}In , the GC prediction is marginally better than the KRK prediction. For ^{104}Cd , the GC prediction shows better agreement when compared with the data. These calculations, however, fail to account for all the details of the experimental excitation functions.

The possibility of ICF reactions contributing to the experimentally measured yields of some of the products was investigated. As stated earlier, we have observed [17] significant yields for the emission of fast alpha particles and other projectile like fragments, having velocity approximately to that of beam, in the present reactions. The fusion of the complimentary fragments with the target will produce intermediate nuclei which will subsequently decay by the particle/gamma emission, depending upon its excitation energy and angular momentum. Since the fusion of ^{15}N with the target to form excited ^{108}Cd is a dominant channel for the present system [17], its subsequent decay by $3n$, $p2n$, and $4n$ emission will enhance the yield of ^{105}Cd , ^{105}Ag , and ^{104}Cd , respectively. The excitation energy of ^{108}Cd has been calculated in the framework of breakup fusion model [23], which varies from 39 MeV to 62.7 MeV for the projectile energy range from 60 MeV to 95 MeV. In this excitation energy range, the cross section for the $3n$, $p2n$, and $4n$ channels will be substantial compared to the $2n$ and pn channels. Contribution to ^{106}Ag from the ICF reactions will be negligible because of this reason. The experimental recoil range data reported in [17], which provide a measure of linear momentum transfer, indicated the role of ICF reactions in con-

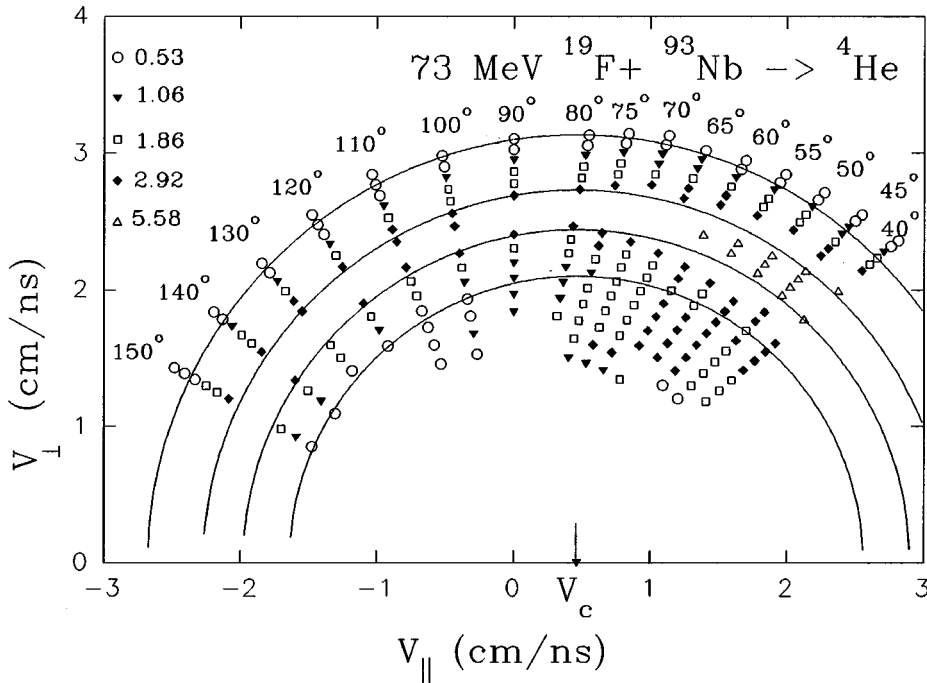


FIG. 3. Velocity contour map of invariant (particle) cross sections $[(d^2\sigma/d\Omega d\epsilon)p^{-1}c^{-1}]_{\text{lab}}$ for alpha emission in the reaction 73 MeV $^{19}\text{F} + ^{93}\text{Nb}$. The axes V_{\parallel} and V_{\perp} denote, the laboratory velocity components of alpha particles parallel and perpendicular to the beam, respectively. The circular arcs are centered on V_c (see arrow), the velocity of center of mass. The invariant cross section magnitudes corresponding to various symbols are indicated in the inset in units of $\mu\text{b}/\text{sr MeV}^2$.

tributing partially to the yield of ^{105}Ag product. The recoil range data for the other products mentioned, however did not show the contributions of the ICF reaction in their production.

In the above analysis, we have not varied any of the parameters of the two level density formulas or the optical model potentials in the PACE2 code in order to remove the remaining discrepancies. As will be shown later, the use of a single level density parameter in describing the emission properties of protons and alphas, itself faces problems. Improvements in the PACE2 calculations to account for such level density effects may remove some of these discrepancies.

In summary, we have measured the experimental excitation functions for nine evaporation residues in the reaction 54 MeV to 95 MeV $^{19}\text{F} + ^{93}\text{Nb}$ and compared the data with two sets of PACE2 predictions, first set using the KRK level density formula and the second set using the GC level density formula. The first set shows some improvements in predicting the excitation functions compared to the second set.

C. Evaporation spectra

The velocity contour map of invariant (particle) cross sections $[(d^2\sigma/d\Omega d\epsilon)p^{-1}c^{-1}]_{\text{lab}}$ provides a picture of overall reaction pattern. We show in Fig. 3 such a map constructed from the measured alpha spectra in the θ_{lab} range from 40° to 150° at 73 MeV bombarding energy. The contours to be expected for the isotropic evaporation from a source moving with the velocity of center of mass, are circular arcs centered on the velocity of the center of mass as shown in Fig. 3. Projectile like fragments from the ICF reactions would manifest themselves as strong deviations from the circular arcs in the direction of the light reaction partner. The data points for the θ_{lab} range from 120° to 150° fall on respective circular arcs thus indicating evaporative emission. Deviations from these arcs particularly due to lower velocities are visible for the θ_{lab} range from 40° to 110° . From similar contour map

for the alpha emission at 95 MeV bombarding energy, it was observed that the deviations are insignificant for the θ_{lab} range from 100° to 160° thus indicating evaporative emission in that angular range. Similar analysis for the proton spectra at both bombarding energies revealed the useful angular range for studying evaporation as from 90° to 160° . The results from particle spectra studies in the above angular ranges, where the dominant source of emission is the evaporation from the compound nucleus, are presented here.

The evaporation from the intermediate nuclei formed in the ICF reactions may also contribute to the measured alpha and proton spectra in the back angles. Maximum percentage contributions of such evaporation were estimated using the measured ICF reaction cross sections (Table III), the breakup fusion model, and the PACE2 code (see Sec. III B). These contributions were found to be less than 5% and 3% for 95 MeV and 73 MeV bombarding energies, respectively.

The measured spectra were converted from the laboratory to the center-of-mass system using the standard Jacobian $v_{\text{c.m.}}/v_{\text{lab}}$, assuming complete momentum transfer. Figures 4–6 show some typical center of mass spectra for the protons and the alpha particles. The symbols indicate the experimental data. The bombarding energy, telescope identification, and laboratory angle at which the telescope was located are indicated in each panel. The statistical error bars are shown in the figures. Similar good statistics data were collected for all the angles where measurements were done. The high energy tail seen in the proton spectra might be due to the background generated by the carbon/oxygen impurity in the target. The energy spectrum of evaporated protons from the nuclei formed in the fusion of projectile with carbon/oxygen impurity will be much flatter compared to that evaporated from the compound nucleus. This is because, the temperatures of the emitting nuclei are quite high in the former case. Therefore, the distortions caused by the background protons are expected to be severe only for very low energy and very high energy part. For the present data on proton evaporation,

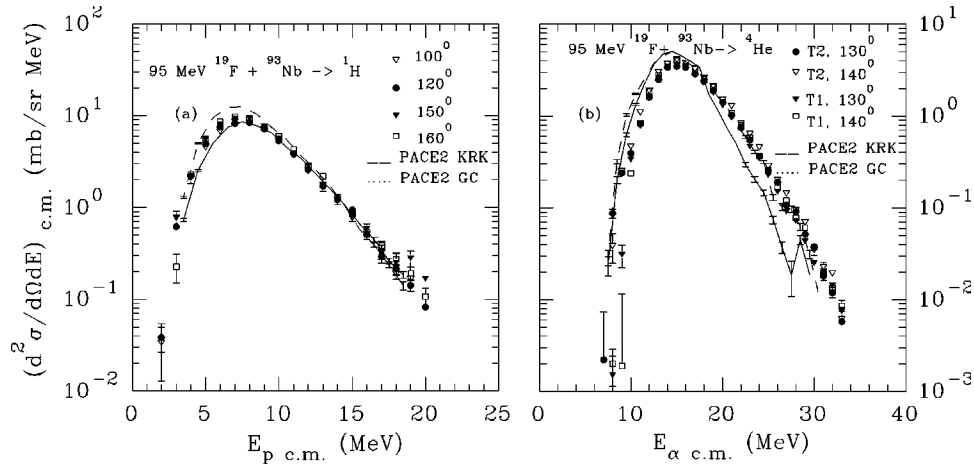


FIG. 4. Experimental and calculated proton (a) and alpha particle (b) spectra in the center of mass system in the reaction 95 MeV $^{19}\text{F} + ^{93}\text{Nb}$. The symbols indicate the experimental data. The particle type, telescope identification, and laboratory angle at which the telescope was located are indicated in each panel. (The proton spectra were measured using T3.) The continuous and dashed lines show the PACE2 predictions with the KRK level density formula and the GC level density formula respectively. The value of a_{LDM} used in the PACE2 calculations was $A/8$. The error bars indicate the statistical error calculated using the number of events generated in each energy bin.

this low and high energy limits were estimated as 4 and 15 MeV, respectively. The alpha spectra are free from such background from light element impurities as also seen in the simulation studies (Sec. II C).

In the present work, we focus on deriving the level density parameters from the experimental spectra. Part of the spectra well above the effective barrier arise predominantly from the first chance emissions [3]. This part is most sensitive to the spin dependent level density [3] and therefore is most suitable for deriving the level density parameter a_{LDM} . The near and below effective-barrier part of the spectra arise mostly from multichance emissions [3]. This part will be influenced by the details of the evaporation barriers in addition to the level densities. Furthermore, the level densities applicable for these emissions are likely to be strongly influenced by the shell effects. Thus many complex factors influence the spectra in the near and below effective-barrier energies.

The normalization usually required while comparing the shape of experimental spectra with that predicted using a statistical model calculation was done in the following way. We matched the experimental and the predicted spectra at

the above effective-barrier part. The PACE2 predicted spectra could be related to the experimental spectra in this way since the former is calculated after consideration of the competition between the decay channels along the cascade. For reasons discussed previously, we have avoided normalization with reference to the yield close to the effective-barrier position.

Figures 4 and 5 show comparison of the experimental spectra, and the predicted spectra for a selected value of $a_{\text{LDM}}=A/8$, for 95 MeV and 73 MeV bombarding energies, respectively. The continuous and dashed lines are the predictions using KRK and GC formulas respectively. The value of a_{LDM} used in obtaining the spectra provides a reasonably good description of ER excitation functions (Sec. III B).

In the case of the proton spectra, both the formulas fit the above barrier part within the experimental errors at both bombarding energies [Figs. 4(a) and 5(a)]. The KRK formula gives a better estimate of the near and below effective-barrier part of the spectra compared to the GC formula.

The situation is different in the case of alpha particles. For the spectra measured at 95 MeV bombarding energy, the formulas give very different predictions for the above

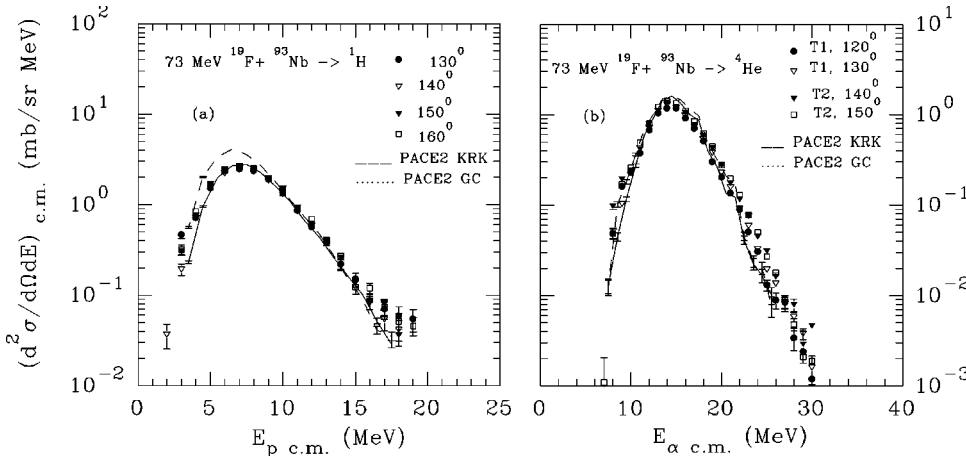


FIG. 5. Experimental and calculated proton (a) and alpha particle (b) spectra in the center of mass system in the reaction 73 MeV $^{19}\text{F} + ^{93}\text{Nb}$. The description and the symbolism are the same as in Fig. 4.

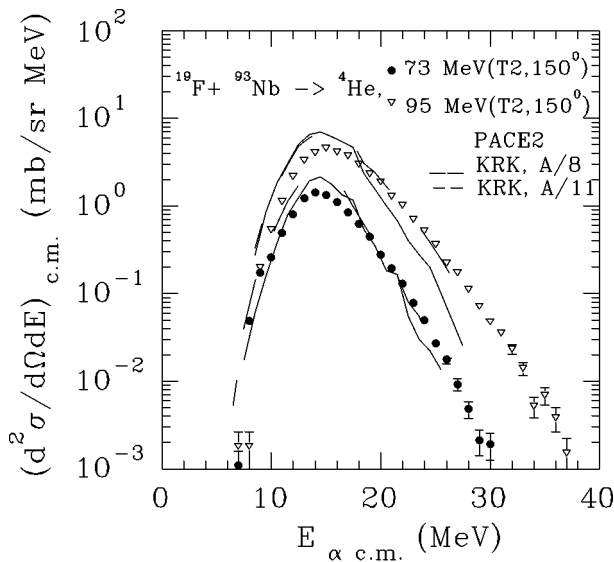


FIG. 6. Experimental and calculated alpha particle spectra in the center of mass system in the reactions 73 MeV, 95 MeV $^{19}\text{F} + ^{93}\text{Nb} \rightarrow ^4\text{He}$. The closed circles and the open inverted triangles indicate the experimental data at 73 MeV and 95 MeV bombarding energies, respectively. The continuous and the dashed lines show the PACE2 predictions using the KRK level density formula with a_{LDM} values $A/8$ and $A/11$, respectively.

effective-barrier part [Fig. 4(b)]. The GC prediction is in agreement with the data for this part whereas the KRK prediction differs substantially. For near and below effective-barrier energies, both the formulas give similar overestimates of the yields. For the spectra measured at 73 MeV bombarding energy the two formulas give very similar predictions [Fig. 5(b)]. The shapes predicted, however, are not smooth. Moreover, they do not show much change for even different values of a_{LDM} . (This is demonstrated in the lower curves of Fig. 6, where PACE2 (KRK) predictions at 73 MeV bombarding energy, with $a_{\text{LDM}}=A/8$ and $A/11$ are shown. The experimental data shown in Fig. 6 were measured using T2 at $\theta_{\text{lab}}=150^\circ$.) The nonsmooth nature of predicted spectra has been noticed in [6] while using another version of PACE2. In [6], it has been suggested that this nature is likely due to the deficiencies in the treatment of rotational energy. Authors of [6] also proposed that the nonsmooth nature will be seen more prominently for the simulations of the decay of compound nuclei formed with low excitation energy but large angular momenta. The reason for this was attributed to the increasing importance of the yrast and near yrast structure, and the gamma strengths, at low excitation energy and high angular momenta.

Keeping aside the 73 MeV bombarding energy alpha predictions for the present, and analyzing only the above effective-barrier part of the proton and alpha spectra, one can observe that the GC formula with $a_{\text{LDM}}=A/8$ fits both proton and alpha spectra. The KRK formula with $a_{\text{LDM}}=A/8$, fits the proton spectra but not the alpha spectra. The value of a_{LDM} required to fit the above effective-barrier part of the alpha spectra while using the KRK formula was found to be $a_{\text{LDM}}=A/11$. The upper curves of Fig. 6 show PACE2 (KRK) predictions for alpha spectra at 95 MeV bombarding energy, using $a_{\text{LDM}}=A/8$ (continuous lines) and $a_{\text{LDM}}=A/11$

(dashed lines). For above effective-barrier energies, $a_{\text{LDM}}=A/11$ shows very good improvement over $a_{\text{LDM}}=A/8$, in fitting the data. Thus in the case of KRK formula, one can observe that, the proton spectra are fitted using $a_{\text{LDM}}=A/8$ but alpha spectra are fitted only by a lower value of $a_{\text{LDM}}=A/11$. (For the above cases, the intervals of a_{LDM} values which gave equally good fits were assessed by trials. A plus-minus of $\sim 10\%$ of the denominator of the respective a_{LDM} , defined these intervals.)

D. Angular distributions

The experimental data on angular distributions of evaporated light particles have been used by many authors [2,4] to obtain information on the spin distribution of the emitter. This is done by assuming spherical shape for the emitter, sharp cutoff transmission coefficients for the emitted particles, and constant temperature approximation for the level density. To decipher the separate roles of transmission coefficients and spin dependent level density in deciding the angular distributions, the study of correlations between the particle emission direction and other measurable properties of emission configurations will be useful. In this subsection, we present experimentally measured correlations between the angular anisotropy and the ejectile energy of the protons and the alpha particles. Corresponding correlations calculated using the statistical model code PACE2 are also presented. A direct comparison between such experimental data and the statistical model necessitates use of Monte Carlo techniques in the calculations. Proper angular momentum couplings at each stage of the cascade emission is imperative to predict the correct angular distribution of the emitted particles and the residual nuclei. The PACE2 code used in the present work uses this procedure and, therefore, is capable of predicting the double differential cross sections of the emitted particles as a function of the angle.

Before obtaining the angular-anisotropy ejectile-energy correlations, let us examine the energy integrated cross sections, both experimental and theoretical, as a function of the center of mass angle. Figures 7(a)–7(d) shows the experimental cross sections as closed circles. The bombarding energy and the type of particle are indicated in each panel. The statistical error bars are smaller than the point size. The energy integrated cross sections as a function of $\theta_{\text{c.m.}}$ predicted using the PACE2 code, with the parameters which reproduce the spectral shapes, are shown as lines. The continuous lines are calculated using the GC formula with $a_{\text{LDM}}=A/8$. For the case of alpha particles at 95 MeV bombarding energy, the KRK prediction with $a_{\text{LDM}}=A/11$ is also shown [dashed line, Fig. 7(a)]. The predicted cross sections (PACE2 GC $A/8$) are in good agreement with the data for the proton (95 MeV) and alpha (73 MeV) cases. (Bombarding energies are shown in the parentheses.) However, for the proton (73 MeV) and alpha (95 MeV) cases, PACE2 (GC $A/8$) overestimates the cross sections. The values of gross anisotropy, $W(180^\circ)/W(90^\circ)$, were obtained by fitting the experimental data to the expression $W(\theta_{\text{c.m.}})=a+b\cos^2\theta_{\text{c.m.}}$ using the least squares method. The gross anisotropies predicted by PACE2 were also calculated in the same manner. The values obtained are tabulated in Table IV. The data and the PACE2 predictions using the GC formula ($a_{\text{LDM}}=A/8$) are in agree-

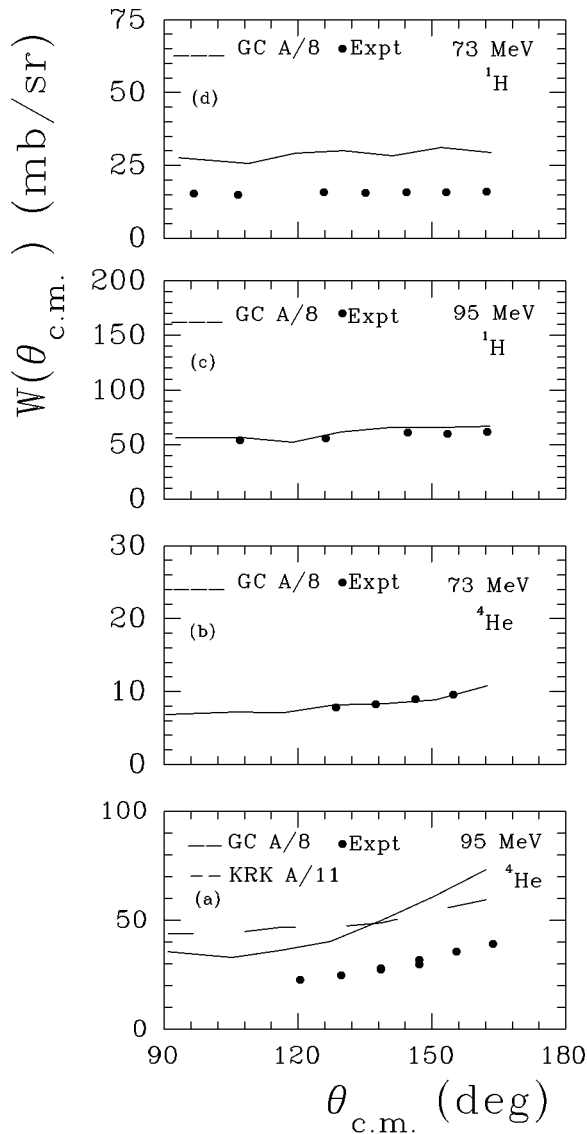


FIG. 7. (a)–(d) Experimental angular distributions of protons and alpha particles in the center of mass system for the reaction $^{19}\text{F} + ^{93}\text{Nb}$. Each panel is labeled with the bombarding energy of the ^{19}F ion. The closed circles indicate the experimental data and the lines indicate the PACE2 predictions. The continuous lines are calculated using the GC formula with $a_{\text{LDM}}=A/8$. The dashed line in (a) is calculated using the KRK formula with $a_{\text{LDM}}=A/11$.

ment for all the cases. The values of proton anisotropy predicted using the KRK formula are in agreement within the error bars. However, for the alpha particle case, the KRK formula calculation severely underestimates the values of anisotropy. The alpha and proton multiplicities, both experimental and PACE2 predicted, are also tabulated in Table IV. The experimental multiplicities were calculated from the angle integrated cross sections. Agreement between the experimental and the PACE2 predicted multiplicities are good only in the cases where the corresponding angular distributions are matched.

We obtained the experimental angular-anisotropy ejectile-energy correlations in the following way. The double differential cross sections at specified values of $E_{\text{c.m.}}$, $d^2\sigma/dE d\Omega|_{E=E_{\text{c.m.}}}$, were obtained as a function of $\theta_{\text{c.m.}}$. The

angular distributions $W(\theta_{\text{c.m.}})|_{E=E_{\text{c.m.}}}$ thus obtained were fitted to the expression $W(\theta_{\text{c.m.}})=a+b\cos^2\theta_{\text{c.m.}}$ using the least squares method and the values of anisotropy $W(180^\circ)/W(90^\circ)|_{E=E_{\text{c.m.}}}$ were determined. For the protons, the range of $E_{p\text{c.m.}}$ was limited from 4 MeV to 15 MeV. As discussed earlier, in this range, the proton background is expected to be much less. For the alphas, the range of $E_{\alpha\text{c.m.}}$ was limited from 10 MeV to 25 MeV.

Figures 8, 9, 10, and 11 show $W(\theta_{\text{c.m.}})/W(90^\circ)$ versus $\theta_{\text{c.m.}}$ for alpha (95 MeV), alpha (73 MeV), proton (95 MeV), and proton (73 MeV), respectively. The legend shows the symbols used for each $E_{\text{c.m.}}$ values. The least squares fits obtained for the angular distributions are also shown as lines. The continuous, long-dashed, dashed, and short-dashed lines correspond to the data indicated by the closed circles, open inverted triangles, closed inverted triangles, and open squares, respectively. The values of $W(180^\circ)/W(90^\circ)$ as a function of $E_{\text{c.m.}}$, derived from these fits are shown in Fig. 12 for both alphas and protons, as closed circles. The qualitative features of the alpha anisotropies are the following. The anisotropies are highest at the highest $E_{\alpha\text{c.m.}}$. As $E_{\alpha\text{c.m.}}$ is decreased, the anisotropy falls. The falling trend halts when the effective-barrier energy is reached. As $E_{\alpha\text{c.m.}}$ is decreased further to subbarrier energies, the anisotropy increases first and then decreases thus forming a peaklike structure. The peaklike structure is more prominent for the 95 MeV data than for the 73 MeV data. The absolute magnitudes are also higher for the 95 MeV data compared to the 73 MeV data. For the protons, the anisotropy is nearly unity at the highest energies. As energy is decreased past the proton evaporation barrier, a peaking behavior in the variation of the anisotropy, though not as prominent as in the alpha case, can be observed for the 95 MeV data. For the protons (73 MeV), the anisotropy is nearly unity throughout the energy range.

A closer inspection of the subbarrier peak in the variation of anisotropy with ejectile energy was carried out by reducing the $E_{\alpha\text{c.m.}}$ bin size to ~ 0.25 MeV. This was to make sure that the observed peak is not a result of some fluctuations in the 1 MeV bins or in the fitting procedure. The results of this investigation for the case of alpha particles measured at 95 MeV bombarding energy is shown in Fig. 13. The correlation shown between $W(164^\circ)/W(121^\circ)$ and $E_{\alpha\text{c.m.}}$ is expected to reflect the correlation between $W(180^\circ)/W(90^\circ)$ and $E_{\alpha\text{c.m.}}$ in good measure. The former was obtained by simply dividing the differential cross sections at $\theta_{\text{c.m.}}\sim 164^\circ$ (corresponding $\theta_{\text{lab}}=160^\circ$) by the differential cross sections at $\theta_{\text{c.m.}}\sim 121^\circ$ (corresponding $\theta_{\text{lab}}=110^\circ$). As anticipated, the nature of correlation in Fig. 12(b) is reproduced in Fig. 13.

The evaporation from the composite nuclei formed in the ICF reactions may have different angular distributions than the complete fusion reactions. Since the percentage contribution of such evaporation to the measured spectra is estimated to be small (Sec. III C), major corrections to the presented results on the anisotropy, due to the ICF reactions, are not expected. Moreover, the composite nuclei spin magnitudes are small and dealigned. As a result, the particles evaporated from such nuclei will have smaller anisotropies. Therefore, the observed increase in the anisotropy for the subbarrier

TABLE IV. Angular anisotropies (A) and multiplicities (M) of protons and alphas in the $^{19}\text{F} + ^{93}\text{Nb}$ system.

Bombarding energy	73 MeV				95 MeV			
	Proton		Alpha		Proton		Alpha	
	A	M	A	M	A	M	A	M
Experimental	1.007 ± 0.025	0.298 ± 0.005	1.64 ± 0.086	0.145 ± 0.005	1.17 ± 0.044	0.62 ± 0.03	2.66 ± 0.35	0.25 ± 0.02
PACE2 GC ($A/8$)	1.128 ± 0.1	0.55	1.55 ± 0.13	0.15	1.263 ± 0.09	0.65	2.4 ± 0.3	0.48
PACE2 KRK ($A/8$)	1.011 ± 0.06	0.89		0.19	1.09 ± 0.08	1.13	1.28 ± 0.17	0.32
PACE2 KRK ($A/11$)		0.89		0.27		1.1	1.36 ± 0.07	0.49

energy range, is not related to the presence of ICF reactions.

Quantitative description of the observed correlations was attempted using the code PACE2 with input parameters which reproduce the spectral shapes. The PACE2 code predicts laboratory energy spectra for the emitted light particles at various angles. The Monte Carlo simulation procedure builds the energy spectra at the forward angles keeping an angular bin size of 10° . For the back angles, the angular bin size is 20° . We chose the forward angle energy spectra since they have smaller angular bin size. The simulated spectra were transformed to the center of mass system. The angular distributions $W(\theta_{\text{c.m.}})|_{E=E_{\text{c.m.}}}$ were obtained as in the experimental case. These angular distributions were fitted to the standard expression $W(\theta_{\text{c.m.}}) = a + b\cos^2\theta_{\text{c.m.}}$ using the least squares method and the values of anisotropy, $W(0^\circ)/W(90^\circ)$ in this case, were obtained. Some systematic deviations from the $a + b\cos^2\theta_{\text{c.m.}}$ behavior could be observed for the very low and very high $E_{\text{c.m.}}$ angular distributions. As a result of these deviations, the error bars on the extracted anisotropies are large.

The anisotropies of the simulated data as a function of the ejectile energy, for both protons and alpha particles and for both bombarding energies, obtained using the above procedure, are given in Figs. 14(a)–14(d). The closed circles indicate the simulated anisotropies obtained using the GC formula with $a_{\text{LDM}} = A/8$. The open inverted triangles shown in Fig. 14(b) indicated the simulated anisotropy obtained using the KRK formula with $a_{\text{LDM}} = A/11$. The continuous lines drawn through the anisotropies of the alpha particles are to guide the eye. The same lines are reproduced on the respective plots in Fig. 12 to facilitate comparison between the experimental and the simulated anisotropies. The experimental and the simulated data on anisotropies have some common features. For the alpha particles, a peak like structure, similar to that of the experimental data, is seen at the subbarrier energies, for both the bombarding energies. In the $E_{\alpha \text{ c.m.}}$ range between 12 MeV and 20 MeV, the trends predicted using the GC formula ($a_{\text{LDM}} = A/8$) are in good agreement with the experimental data for both bombarding energies. However, for the subbarrier energy range, the GC formula ($a_{\text{LDM}} = A/8$) predicts much larger anisotropies compared to the experimental data. The height of the subbar-

rier peak predicted using the KRK formula ($a_{\text{LDM}} = A/11$) matches with the experimental data [Fig. 12(b)]. However, in this case, the anisotropies at high $E_{\text{c.m.}}$ are under estimated. The subbarrier peak positions are predicted at about 10 MeV by both formulas which are less than the experimental value by about 1.5 MeV. For the protons, because of the large error bars, no clear conclusion regarding the agreement between the predicted and experimental trends can be drawn. The continuous lines drawn on Figs. 12(c) and 12(d) are indicative of the gross anisotropies calculated using the GC formula with $a_{\text{LDM}} = A/8$.

IV. DISCUSSION

We have attempted to interpret our experimental data on ER excitation functions, evaporated proton and alpha energy and angular distributions, and angular-anisotropy ejectile-energy correlations using two different kinds of PACE2 [9] calculations. The first one uses the Kataria-Ramamurthy-Kapoor (KRK) level density formula [11]. The second one uses the modified Gilbert-Cameron (GC) level density formula [9,10]. The first calculation provided a better description of the ER excitation functions compared to the second. The value of the parameter a_{LDM} used while fitting the excitation functions was $A/8$. [A consistent set of other input parameters were used in the calculations (Sec. III)]. The spectral shapes of the evaporated protons at the above effective-barrier energies were also well described by this calculation using the same set of input parameters. However, the spectral shape of evaporated alphas at the above effective-barrier energies, could be described only by a lower value of input parameter $a_{\text{LDM}} = A/11$. The second calculation, on the other hand, describes the proton and alpha spectral shapes at above effective-barrier energies reasonably well with $a_{\text{LDM}} = A/8$.

A similar situation regarding the proton and alpha spectral shapes is reported in [6]. Experimental energy spectra of the light charged particles [24] evaporated from ^{117}Te compound nucleus at excitation energy 106 MeV were analyzed using another version of PACE2 [6,25]. This experimental system is quite similar to the system studied in the present work. The excitation energy, however, is slightly higher than that of the

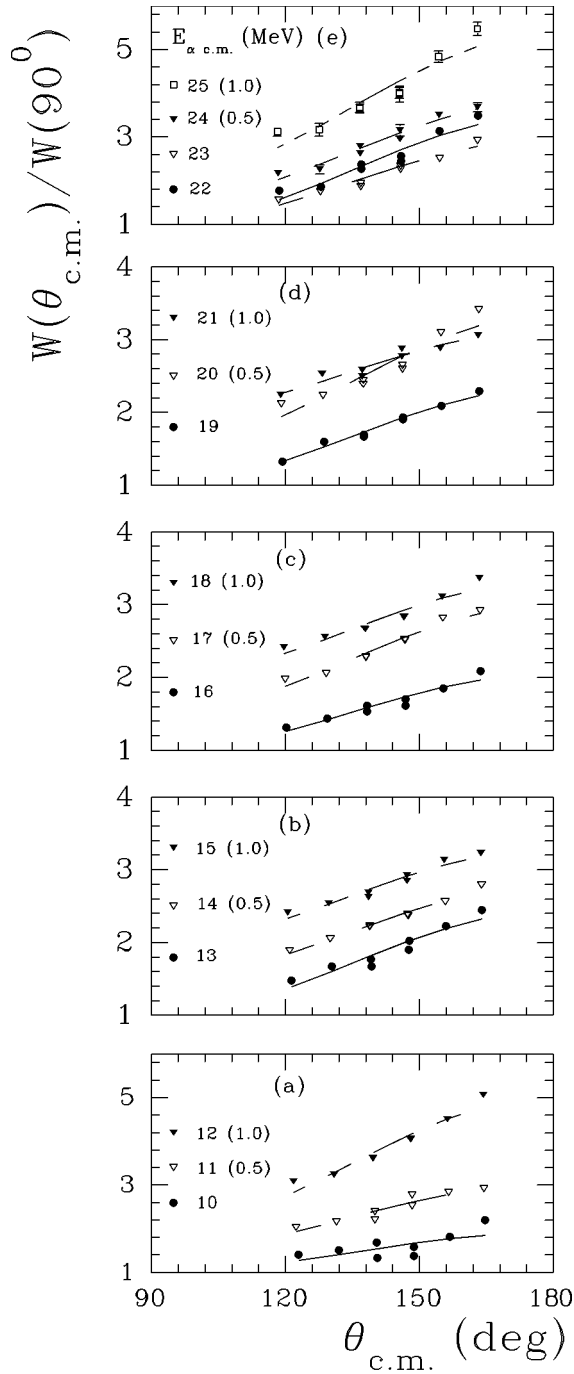


FIG. 8. (a)–(e) Experimental angular distributions in the center of mass system, of the alpha particles from the reaction 95 MeV $^{19}\text{F} + ^{93}\text{Nb}$, for various $E_{\alpha \text{ c.m.}}$ bins of size 1 MeV. The symbols used for different bins, and the mean energy corresponding to each bin are indicated in the panels. The continuous, long-dashed, dashed, and short-dashed lines are least squares, fits to the data, shown by closed circles, open triangles, closed triangles, and open squares respectively, using the expression $W(\theta_{\text{c.m.}}) = a + b \cos^2 \theta_{\text{c.m.}}$. In some cases, the data and fits have been shifted along the vertical axis by the amount indicated in the parentheses.

95 MeV bombarding energy case. The version of the PACE2 [25] uses a Fermi gas form for the level density with level density parameter and back shift varying from nucleus to nucleus. The level density parameter used was in the range $A/7$ to $A/9$. Their results show a good agreement between the

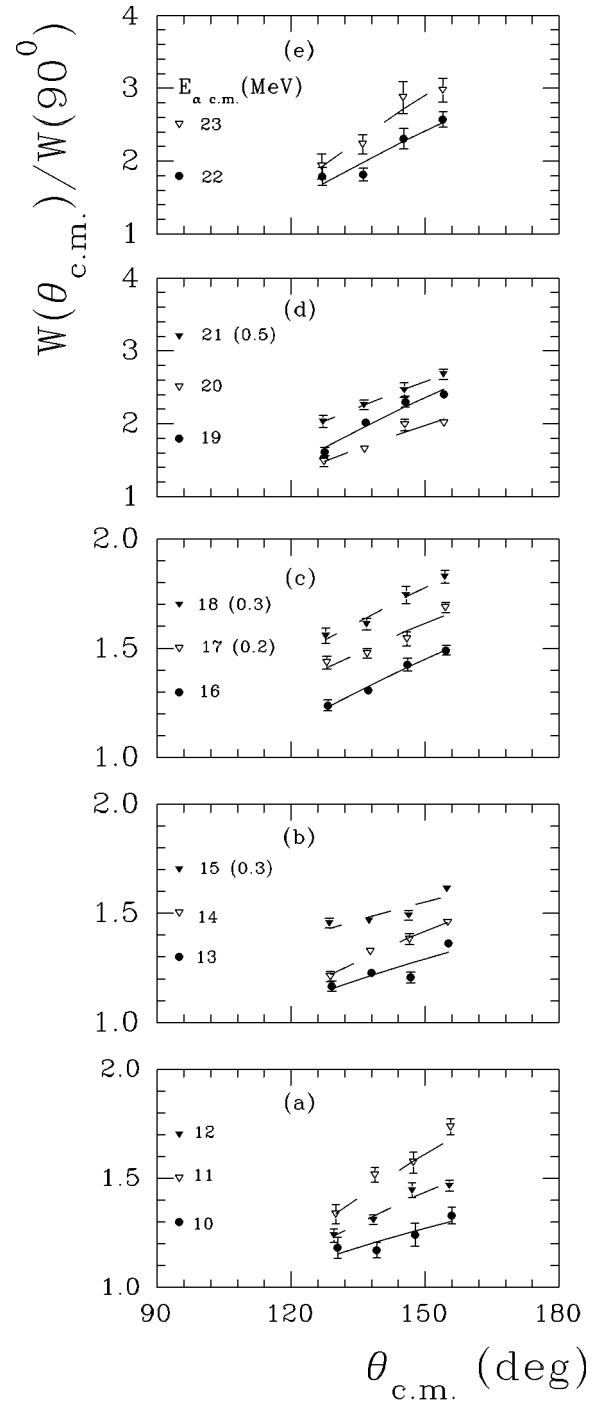


FIG. 9. (a)–(e) Experimental angular distributions in the center of mass system, of alpha particles of various $E_{\alpha \text{ c.m.}}$ as in Fig. 8, but from the reaction 73 MeV $^{19}\text{F} + ^{93}\text{Nb}$. The description and the symbolism are the same as in Fig. 8.

experiment and the prediction for the case of proton spectral shape. However, for the case of alphas, the predicted spectral shape shows much larger slope for the above effective-barrier part, compared to the experimental data. The comparison between the experimental and predicted spectral shapes [6] is very similar to the comparison between the present data and the continuous line as shown in Fig. 4(b). However, in Ref. [6], no attempts were made to vary the level density parameter to improve the alpha spectra fit as

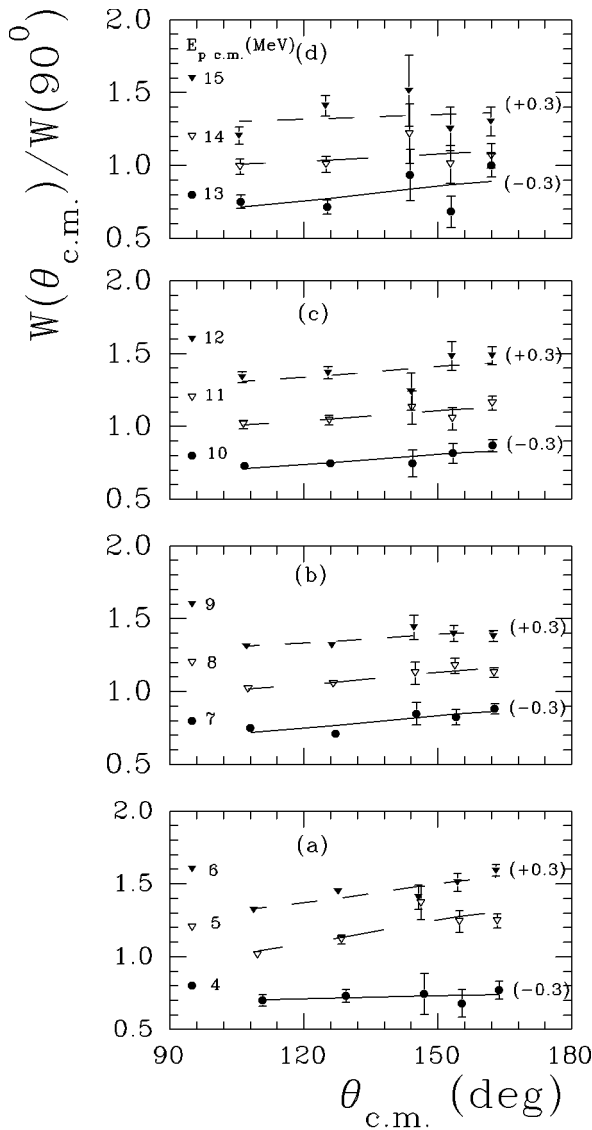


FIG. 10. (a)–(d) Experimental angular distributions in the center of mass system, of protons of various $E_{p \text{ c.m.}}$ from the reaction 95 MeV $^{19}\text{F} + ^{93}\text{Nb}$, for various $E_{p \text{ c.m.}}$ bins of size 1 MeV. The description and the symbolism are the same as in Fig. 8.

has been done in the present work (Fig. 6 upper lines, Sec. III C)

The alpha particle angular-anisotropy ejectile-energy correlations, particularly at the sub-barrier energies, seem to be quite sensitive to the statistical model parameters (Sec. III D). Experimental angular-anisotropy ejectile-energy correlations for protons and alphas evaporated from $^{75}\text{Br}^*$ (88) compound nucleus for the above effective-barrier energies are given in [26]. (Number in the parentheses indicate excitation energy of the compound nucleus in MeV.) The qualitative features of the present alpha data for the above effective-barrier energies are very similar to that presented in [26]. For the protons, present data ($E_p \geq 5$ MeV, 95 MeV bombarding energy) shows similar features as in [26]. Nicolis *et al.* [2] have measured experimental angular correlation between the estimated spin direction and the direction of emission of the alpha particles of a given $E_{\alpha \text{ c.m.}}$, as a function of gamma multiplicity for the compound nuclei

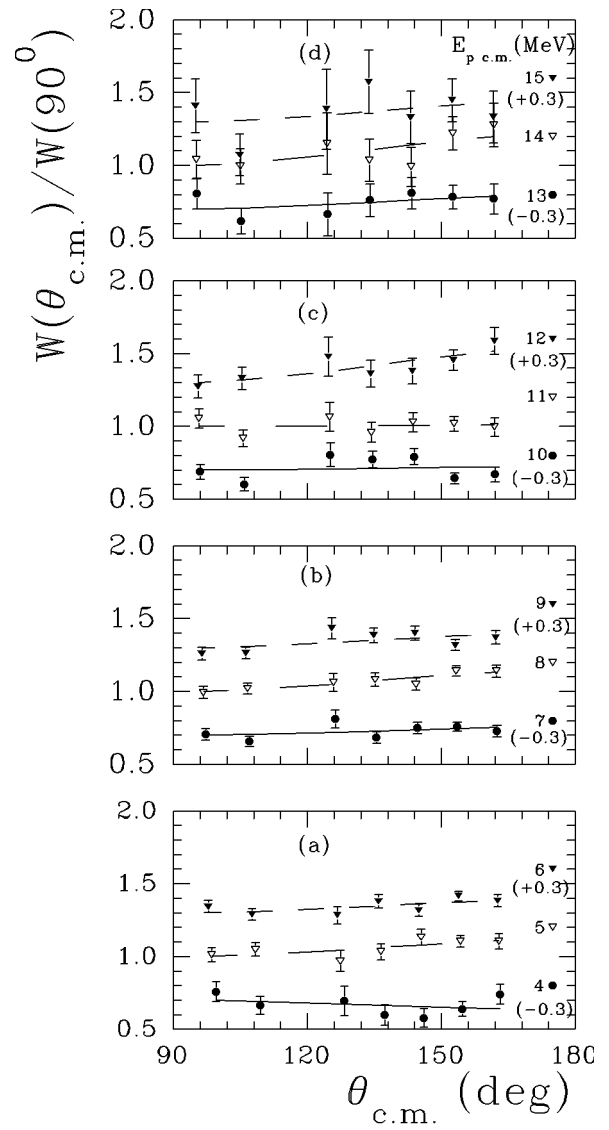


FIG. 11. (a)–(d) Experimental angular distributions in the center of mass system, of protons of various $E_{p \text{ c.m.}}$ as in Fig. 10 but from the reaction 73 MeV $^{19}\text{F} + ^{93}\text{Nb}$. The description and the symbolism are the same as in Fig. 8.

$^{110}\text{Sn}^*(94)$, $^{114}\text{Sn}^*(80)$, $^{138}\text{Nd}^*(82)$, $^{164}\text{Yb}^*(67)$, and $^{170}\text{Yb}^*(135)$. Their results suggest that the angular anisotropy and the ejectile energy are correlated in a similar way as found in the present study for the above effective-barrier energies. For $^{114}\text{Sn}^*(80)$ system, in the subbarrier region, no clear indication for an increase in the anisotropy was observed. However, the data for the two lowest and the highest gamma multiplicity bins indicate some increase. For $^{110}\text{Sn}^*(94)$ system, significantly lower anisotropies for all the multiplicity bins were observed.

In Ref. [2], qualitative trends of the observed correlations for Sn isotopes have been explained in terms of the combined effects of the transmission coefficients (T_l) and the level densities. It has been argued [2] that as $E_{\alpha \text{ c.m.}}$ is increased from the barrier energies, the values of T_l increase for the larger l values leading to monotonically increasing anisotropies. Similarly, as $E_{\alpha \text{ c.m.}}$ decreased past the barrier, the number of l waves with $T_l \neq 0$ diminishes rapidly leading

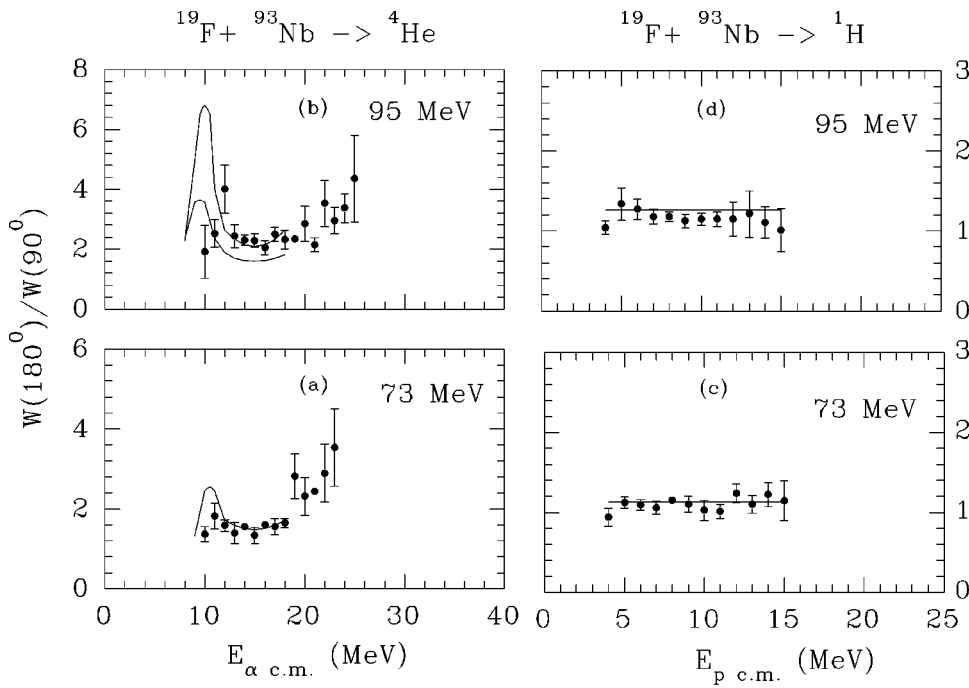


FIG. 12. (a)–(d) Experimental angular-anisotropy ejectile-energy correlations of protons and alpha particles from the reactions 73 MeV, 95 MeV $^{19}\text{F} + ^{93}\text{Nb}$. The continuous lines shown indicate the corresponding correlations calculated using PACE2. See the text for details.

eventually to isotropy. Quantitative description of the observed correlations effects has also been carried out in [2] using another version statistical model code PACE2. This calculation reproduced the trend as well as absolute magnitudes of the anisotropies for the case of ^{114}Sn . The sensitivity of the calculated anisotropy values in statistical model parameter changes, particularly the yrast line and the gamma strengths were examined in [2]. Their study suggests that the anisotropy values in the subbarrier $E_{\alpha \text{ c.m.}}$ range may deviate from the trend expected from the smooth variation of the T_l values alone. The structure effects can influence the anisotropy values especially in the subbarrier range. This has been demonstrated in the present analysis also in the form of a dependence on the level density formalism used. The peak like structure observed for the subbarrier energy show the evidence for the role of level densities. The anisotropy values calculated using the two formulas differ maximum at the sub-barrier energies. Failure of these calculations in completely reproducing the experimental trend may be indicating some inadequacies of the transmission coefficient and/or the spin dependent level density prescriptions used.

It is instructive to examine the average properties of the scission configurations responsible for the alpha emission of various $E_{\alpha \text{ c.m.}}$. (The combination of the phase space factors and the transmission coefficients defines the scission configuration.) The high energy tail of the cumulative spectrum is understood to have originated from first chance emissions from high spin states [3] and the corresponding scission configurations possess high spin. As $E_{\alpha \text{ c.m.}}$ is decreased to subbarrier energies, average spin decreases [2]. The average excitation energy of the scission configuration as well as transmission coefficients are also decreased as $E_{\alpha \text{ c.m.}}$ is decreased [2,3]. As a result, the shell structure/discrete level effects will start influencing the emission at subbarrier $E_{\alpha \text{ c.m.}}$ [2]. These properties resemble the average scission configuration properties of heavy ion induced fission reactions in the following way. For reactions induced by bombarding energies much above the entrance channel barrier energies, the

scission configuration will have on the average high spin and moderate excitation energy. As bombarding energy is decreased, these quantities also decrease. The transmission coefficients in the fission case are related to the velocity of the system along the fission coordinate and the effective separation [27,28]. For fission after full equilibration, the average velocity of the system along the fission coordinate and the effective separation are not expected to change significantly with the bombarding energy. As a result, the average transmission coefficients also will not change significantly. Thus for the fission after equilibration, phase space factors guide the angular anisotropy behavior. This has been demonstrated experimentally for a number of heavy ion induced fission reactions [27]. Experimental values of the fragment anisotropy decrease as the bombarding energy is decreased from

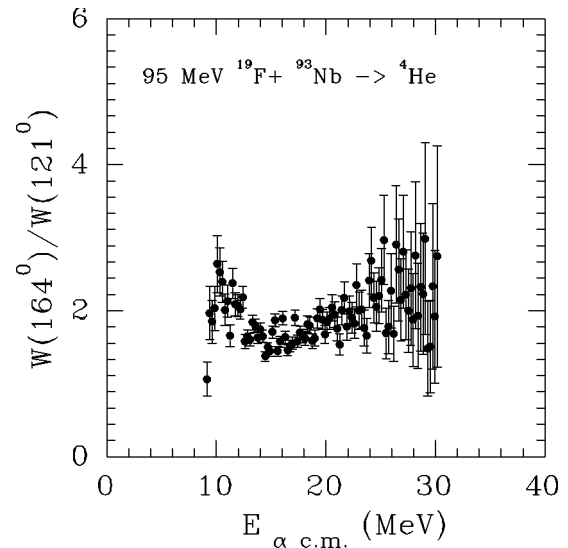


FIG. 13. Experimental $W(164^\circ)/W(121^\circ)$ as a function of the ejectile energy of the alpha particles from the reaction 95 MeV $^{19}\text{F} + ^{93}\text{Nb}$.

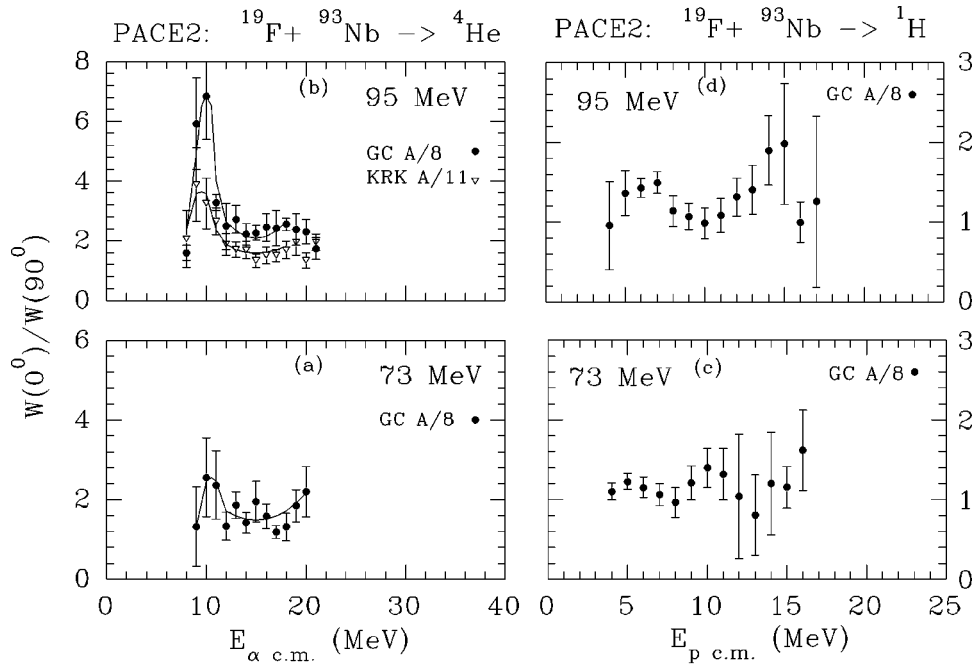


FIG. 14. (a)–(d) Theoretical angular-anisotropy ejectile-energy correlations of protons and alpha particles from the reactions 73 MeV, 95 MeV $^{19}\text{F} + ^{93}\text{Nb}$ calculated using the PACE2. The closed circles are calculated using the GC formula with $a_{\text{LDM}}=A/8$. The open triangles in (b) are calculated using the KRK formula with $a_{\text{LDM}}=A/11$. The continuous lines drawn in (a) and (b) are to guide the eye.

higher energies to near barrier energies. Anisotropies calculated based on the phase space factors of the scission configurations, reproduce the experimental trend [27].

Recently, for some systems, an anomalous increase (a peaklike structure) in the variation of anisotropy in the sub-barrier bombarding energy range was observed [29,30]. The explanation given was in terms of quasifission model [29,30]. If quasifission events are present for these reactions in the subbarrier bombarding energy range, then the fragments from these events will have only low velocities in the fission coordinate. The reason for the low velocities is the nature of the collision, i.e., stopping of the projectile and then reseparation before full equilibration. The effective separations in quasifissions will be larger than that of equilibrium fissions [29,30]. On account of the low velocities and the large separations, the transmission coefficients in the quasifissions may deviate from the usual values. The combined effects of the reduced phase space volume and the unusual behavior of transmission coefficients may lead to some effects similar to the shell structure effects and boost the anisotropy values in the subbarrier energy range, as in the case of subbarrier alpha evaporation. It may be added that such a behavior of the anisotropies need not be universal since the structural effects depend on the specific aspects of the nuclei under study. Better theoretical understanding of these aspects, and more accurate measurements of the anisotropy-energy correlations in the alpha evaporation and fission, may unravel the scission configurations in the two cases.

V. SUMMARY AND CONCLUSIONS

We have measured the evaporation residue (ER) excitation functions of the reaction $^{19}\text{F} + ^{93}\text{Nb}$ leading to the compound nucleus $^{112}\text{Sn}^*$, in the bombarding energy range between 54 and 95 MeV, using the off-line recoil catcher

technique. Measurements of the evaporated proton and alpha particle energy spectra and angular distributions, for the same system at bombarding energies 73 and 95 MeV, were carried out using silicon telescopes. The experimental correlations between the angular anisotropy and the ejectile energy, of the evaporated protons and alphas, were derived from the set of data. We have also measured the elastic scattering angular distributions at 73 and 95 MeV bombarding energy for the $^{19}\text{F} + ^{93}\text{Nb}$ system and the data were analyzed using the optical model, and the values of ΔL were extracted, which characterizes the distribution of angular momentum in the incident channel.

The measured ER excitation functions, energy and angular distributions, and angular-anisotropy ejectile-energy correlations of protons and alpha particles were compared with the predictions of the statistical model code PACE2, making use of two level density formalisms; one due to Gilbert and Cameron (GC) [9,10], and the other due to Kataria, Ramamurthy, and Kapoor (KRK) [11]. The better agreement in predicting the ER excitation functions using the KRK formula has been attributed to the realistic way by which this formula treats the shell corrections. However, a complete description of the energy spectra and angular distributions of the protons and alphas could not be achieved by using either formula. The part of the proton spectra above the effective-barrier was reproduced within the experimental errors, by both the formulas. The level density parameter used in the proton spectra calculations and the ER excitation function calculations was $a_{\text{LDM}}=A/8$. In the case of alpha particle spectra, only GC formula could reproduce the above barrier part with $a_{\text{LDM}}=A/8$. The KRK formula, on the other hand, could reproduce this part only with a lower value of $a_{\text{LDM}}=A/11$.

The angular-anisotropy ejectile-energy correlations measured in the present work revealed high values of the angular anisotropy for the sub-barrier ejectile energies particularly

for the alpha particles. Corresponding correlations obtained from the PACE2 calculations also showed high values of the angular anisotropy for the subbarrier alpha emissions, and these are shown to be sensitive to the crucial parameters of the statistical model. Similarities between these correlations, and the recently observed peak and/or increase in the variation of the fragment anisotropy with the bombarding energy in the subbarrier range for some heavy ion induced fission reactions, have been discussed.

The remaining discrepancies between the present experimental data and the statistical model calculations could be arising due to the inadequacies in the treatment of the spin dependent level densities and the transmission coefficients

for the emission channels. The presence of incomplete fusion reactions also could be a reason for the observed discrepancies.

ACKNOWLEDGMENTS

We are thankful to the operating staff of the Pelletron accelerator facility at TIFR for making available the required beams. Particular appreciation is due to Aruna Nijasure for her contributions in the initial stage of this work. We would like to acknowledge discussions with Dr. S. Kailas and Dr. A. V. R. Reddy. We are thankful to Dr. S. S. Kapoor for his encouragement and many valuable suggestions during the course of this work.

-
- [1] R. G. Stokstad, in *Treatise on Heavy Ion Science*, edited by D.A. Bromley (Plenum Press, New York, 1985), Vol. 3, p. 83.
- [2] N. G. Nicolis *et al.*, *Phys. Rev. C* **41**, 2118 (1990).
- [3] J. R. Huizenga, A. N. Behkami, I. M. Govil, W. V. Schroder, and J. Toke, *Phys. Rev. C* **40**, 668 (1989).
- [4] G. L. Catchen, M. Kaplan, J. M. Alexander, and M. F. Rivet, *Phys. Rev. C* **21**, 940 (1986).
- [5] D. Hilscher and H. Rossner, *Ann. Phys. (Paris)* **17**, 471 (1992).
- [6] A. Chbihi, L. G. Sobotka, N. G. Nicolis, D. G. Sarantites, D. W. Stracener, Z. Majka, D. C. Hensley, J. R. Beene, and M. L. Halbert, *Phys. Rev. C* **43**, 666 (1991).
- [7] J. Gomez del Campo *et al.*, *Phys. Rev. C* **53**, 222 (1996).
- [8] M. Thoennessen, E. Ramakrishnan, J. R. Beene, F. E. Bertrand, M. L. Halbert, D. J. Horen, P. E. Mueller, and R. L. Varner, *Phys. Rev. C* **51**, 3148 (1995); J. J. Gaardhoje, C. Ellegaard, and B. Herskind, *Phys. Rev. Lett.* **53**, 148 (1984).
- [9] PACE2 computer code, A. Gavron, *Phys. Rev. C* **20**, 230 (1980).
- [10] A. Gilbert and A. G. W. Cameron, *Can. J. Phys.* **43**, 1446 (1965).
- [11] S. K. Kataria, V. S. Ramamurthy, and S. S. Kapoor, *Phys. Rev. C* **18**, 549 (1978).
- [12] R. Bass, *Phys. Rev. Lett.* **39**, 265 (1977).
- [13] L. C. Northcliffe and R. F. Schilling, *Nucl. Data Tables* **A7**, 233 (1970).
- [14] U. Reus and W. Westmeier, *At. Data Nucl. Data Tables* **2**, 1 (1983).
- [15] D. R. Chakraborty, V. M. Datar, Suresh Kumar, E. T. Mirgule, H. H. Oza, and U. K. Pal, *Phys. Rev. C* **51**, 2942 (1995).
- [16] P. Schwandt, Indiana University Cyclotron Facility, SNOOPY Computer Programme: Optical Potential Model Code for Elastic Scattering Analysis, Indiana University Cyclotron Report (1988).
- [17] B. S. Tomar, A. Goswami, G. K. Gubbi, A. V. R. Reddy, S. B. Manohar, Bency John, and S. K. Kataria, submitted to *Phys. Rev. C*.
- [18] J. R. Huizenga and G. Igo, *Nucl. Phys.* **29**, 462 (1961).
- [19] F. G. Perey, *Phys. Rev.* **131**, 745 (1963).
- [20] D. Willmore and P. E. Hodgson, *Nucl. Phys.* **55**, 673 (1964).
- [21] P. M. Endt, *At. Data Nucl. Data Tables* **26**, 47 (1981).
- [22] S. K. Kataria, V. S. Ramamurthy, M. Blann, and T. T. Komoto, *Nucl. Instrum. Methods Phys. Res. A* **288**, 585 (1990).
- [23] J. Wilczynski, K. Siwek-Wilczynska, J. Van Driel, S. Gonggrijp, D. C. J. M. Hageman, R. V. F. Janssens, J. Lukasiak, R. H. Siemssen, and S. Y. Van der Werf, *Nucl. Phys.* **A373**, 109 (1982).
- [24] J. Galin, B. Gatty, D. Guerreau, C. Rousset, U. C. Schlotthauer-Voos, and X. Tarrago, *Phys. Rev. C* **9**, 1113 (1974); **9**, 1126 (1974).
- [25] Code PACEX, N. G. Nicolis and J. R. Beene (unpublished); extended version of the code PACE2 [9]; D. W. Lang, *Nucl. Phys.* **77**, 545 (1966); W. Dilg, W. Schantl, H. Vonach, and M. Uhl, *Nucl. Phys.* **A217**, 269 (1973).
- [26] R. C. Reedy, M. J. Fluss, G. F. Herzog, L. Kowalski, and J. M. Miller, *Phys. Rev.* **188**, 1771 (1969).
- [27] H. Rossner, J. R. Huizenga, and W. U. Schroder, *Phys. Rev. C* **33**, 560 (1986), and references therein.
- [28] K. Pomorski, J. Bartel, J. Richert, and K. Dietrich, *Nucl. Phys.* **A605**, 87 (1996).
- [29] D. J. Hinde, M. Dasgupta, J. R. Leigh, J. P. Lestone, J. C. Mein, C. R. Morton, J. O. Newton, and H. Timmers, *Phys. Rev. Lett.* **74**, 1295 (1995).
- [30] N. Majumdar, P. Bhattacharya, D. C. Biswas, R. K. Choudhury, D. M. Nadkarni, and A. Saxena, *Phys. Rev. Lett.* **77**, 5027 (1996); J. P. Lestone, A. A. Sonzogni, M. P. Kelly, and D. Prindle, *Phys. Rev. C* **55**, R16 (1997); J. C. Mein, D. J. Hinde, M. Dasgupta, J. R. Leigh, J. O. Newton, and H. Timmers, *ibid.* **55**, R995 (1997).
- [31] H. Geissel, Y. Laichter, W. F. W. Schneider, and P. Armbruster, *Nucl. Instrum. Methods* **215**, 329 (1983).
- [32] J. T. Routti, University of California, Lawrence Berkeley Laboratory Report UCRL-19452, 1969.